

Research Article

# Mapping Ground Displacement Near the Former Dhrovjani Salt Mine Using Differential Radar Interferometry

Pietro Belba\*, Jorgaq Thanas

<sup>1</sup> Department of Mineral Resources Engineering, Polytechnic University of Tirana, Albania

\*[pietro.belba@fgjm.edu.al](mailto:pietro.belba@fgjm.edu.al)

---

## Abstract

Remote sensing and Geographic Information Systems (GIS) are essential tools for estimating and monitoring land subsidence. Over the past fifteen years, various applications of deformation analysis using Differential SAR Interferometry (DInSAR) have been developed. This study employs the two-pass interferometric method to assess ground deformation near a closed rock salt mine in southern Albania. By analyzing two radar images captured at different times from the same satellite position, we measure phase differences to create an interferogram. This interferogram illustrates phase shifts that can be converted into a ground deformation map, indicating surface changes in the radar line-of-sight (LOS) direction. The methodology, termed differential interferometry, allows for detecting relative surface deformation with high precision. The interferometric processing workflow, consisting of core registration, interferogram generation, phase unwrapping (executed using SNAPHU), and displacement mapping, showcases the method's effectiveness in capturing and analyzing surface movement. Accurate interpretation at each phase is vital for reliable results.

**Keywords:** InSAR, Interferogram; DInSAR, Phase Unwrapping

## INTRODUCTION

Subsidence is the downward movement of the ground surface, caused either by natural processes or human activities such as mining. This phenomenon has been observed in various European countries such as Britain, Germany, and Spain [1-3]. In areas where the ground is covered by layers of soluble rocks like evaporates, subsidence can lead to rapid and noticeable surface changes, often resulting in damage to structures. Enclosed depressions, or karst landforms, are a common feature in such regions, with subsidence dolines (sinkholes) developing quickly.

Subsidence can cause ground deformations, cracks, and rapid changes in water levels. The most significant surface movements usually happen in the first 18 months after mining, but some damage may appear much later, even years after the mine has closed. Abandoned mines can remain hazardous, as their entrances may collapse, leading to

further risks. These slow shifts in the ground, even small ones, can be detected and must be closely monitored to prevent accidents and property damage [4-7].

Traditional methods like GPS surveying and levelling were used to detect and measure surface deformations, but these techniques provide limited data [8-10]. Nevertheless, the adoption of satellite-based SAR Interferometry (InSAR) has significantly advanced the monitoring process. InSAR offers wide-area coverage and precise measurements, even without ground instruments [11-14]. Over the last 15 years, DInSAR emerged as a technique to measure surface displacements with high precision, which significantly enhances the ability to monitor ground movements. DInSAR has been applied successfully in various fields, such as seismology, volcanology, and glaciology, but less so for landslide detection due to the loss of signal coherence in such areas [15-23]. Numerous publications have addressed ground deformation phenomena, including subsidence and uplift resulting from fluid withdrawal, construction operations, geothermal activity, and related processes [24, 25].

For this study, the goal is to assess ground movements near a closed rock salt mine in Dhrovjan, southern Albania. The land there began to sink in March 2021, with a pit that was about 20 square meters in area and 4 meters deep. The soil was soft and prone to sinking, especially after heavy rains. A second pit appeared in April 2021, about 10 meters away from the first. An interferogram is created by combining two satellite images from March and April. This process, called differential interferometry, allows us to isolate the deformations by subtracting phase shifts due to topography. The result is a map that shows how the surface has moved between these two dates.

The main aim is to track and model the ground motion from March to December 2021 in the area around the closed mine, using InSAR and DInSAR techniques. By refining the data through post-processing, such as removing inaccurate values, we can get more precise measurements of the ground's displacement. This approach promises to provide more detailed information about terrain changes over time.

This study is important because it applies remote sensing to identify deformations occurring in areas near mines. It will also serve as a starting point for the application of other, more advanced remote sensing techniques.

## **MATERIALS**

### *Study area*

The first rock salt mine in Albania was located in Dhrovjan, in the Saranda district. The salt body there consists of about 80-82% halite (NaCl) and other materials like deltiline, anhydrite, and dolomite. It has a lens shape, with a thickness of 120-130 meters, and is found between Eocene silica deposits. The salt is mainly light ash, dark ash, and reddish. The people of nearby villages like Dhrovjan, Muzina, and Krongj used to collect pure salt from salty springs in the area.

Research conducted in the 1970s revealed the source of the salt, and in 1970, an open-pit mine was opened in Dhrovjan. The mining method used was called the room and pillar system. The mine produced around 75-80 thousand tons of salt per year, which was mainly used as a raw material for the caustic soda factory in Vlora. The mine continued operating until 1980 and was renovated for about 10 more years before it closed.

Today, if you travel past the Bistrice Hydroelectric Power Plant and begin ascending the Muzina Pass, you will come across some ruins near the village of Dhrovjan. These ruins were once the offices and silos of the mine's administration and workers, marking the site of one of Albania's largest and only rock salt mines, see Figure 1.

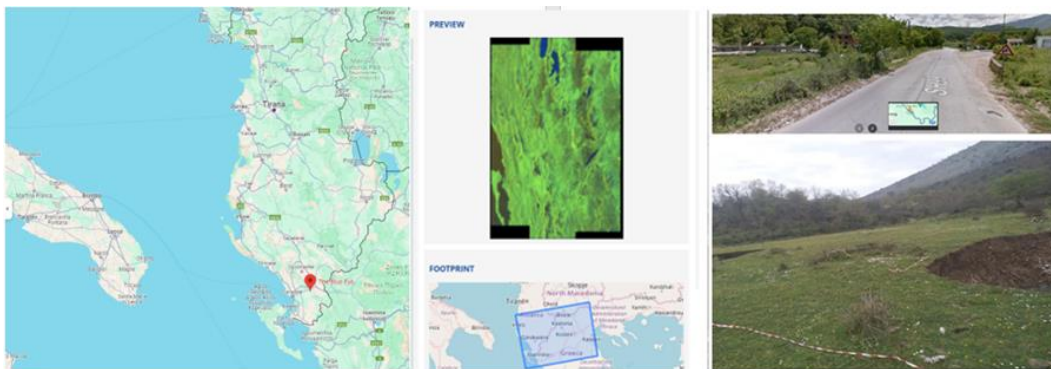


**Figure 1.** Region of Interest in Google Maps and Copernicus Hub. Salt mine on the way to the Muzina pass, while a little higher on the right of the road are the two pits opened in March and April 2021

### **Dataset**

The data for this study were acquired through the European Space Agency's (ESA) Copernicus program, specifically from the Sentinel-1 satellite mission. This satellite system uses a C-Band Synthetic Aperture Radar (SAR) operating at a central frequency of 5.405 GHz. It consists of two satellites in polar orbit, allowing for radar imaging to be captured both during the day and at night.

Radar images are created by analysing the echoes that bounce back to the satellite's antenna after it emits microwave pulses, a process known as backscattering. The radar image is formed based on two axes: the azimuth and range axes. The azimuth axis is aligned with the direction the satellite is traveling, while the range axis is perpendicular to the satellite's motion, measuring the intensity of the returned signal.

This method allows for the mapping of physical surface characteristics like roughness, moisture, and structure. An important advantage of radar imaging is that it can capture data even through cloud cover and regardless of daylight conditions.

In this study, we utilized SAR images acquired by Sentinel-1 using the Terrain Observation by Progressive Scan (TOPS) mode, which is commonly employed for wide-area monitoring. The data were processed to Level-1 Single Look Complex (SLC) format. Each image consists of three sub-swaths, with each sub-swath containing nine bursts. The selected images were chosen to ensure complete coverage of the region of interest.

The key to this study was identifying an appropriate interferometric pair of images with one image obtained before the event and the other acquired afterward, facilitating comparative analysis. The first image was taken on March 2, 2021 (10 days before the main event), and the second was captured on December 27, 2021 (9 months after the event). Both images were taken during ascending passes of the satellite.

### *Extraction of data*

For this study, we used a pair of Sentinel-1 images covering the area around the former rock salt mine in Dhrovjan, near the Blue Eye in Saranda, Albania. To analyze ground displacement, we generated an interferogram using the Sentinel-1 Toolbox. This process is computationally intensive and can be time-consuming to complete.

The first step was to search for the relevant Sentinel-1 data using the Copernicus Data Space. To do this, we accessed the Copernicus browser [26].

Using the search parameters—Sentinel-1, IW mode, level-1 SLC, and VV polarization—we identified two images: one taken before the subsidence event and the other after. These images were selected for their relevance to the study of ground motion and deformation in the area of interest, and we presented them in Figure 2.

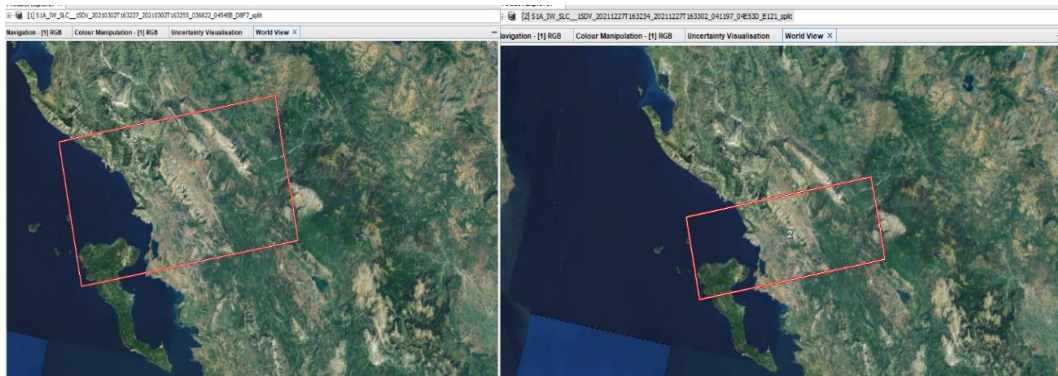


**Figure 2.** Two images before the subsidence (02/03/2021) & after the subsidence (27/12/2021).

## **METHODS**

We applied the two-pass interferometry method using a pair of radar images to measure the phase difference between them. This process produces an interferogram, which visualizes the phase shifts between the two acquisitions. These phase shifts can then be converted into a ground deformation map, revealing surface changes over time.

The SAR (Synthetic Aperture Radar) signal contains two components: amplitude and phase. The radar phase is influenced by the distance between the satellite and the ground target. Interferometric Synthetic Aperture Radar (InSAR) is a remote sensing technique used to map ground deformation by analysing radar images of the Earth's surface captured by orbiting satellites.

InSAR operates by comparing the phase differences between two radar images, which are influenced by both surface topography and any ground deformation. By removing the

phase shifts caused by topography, the difference between the two images will highlight surface deformation that occurred between the two acquisition dates. This technique is called Differential Interferometry. The process involves phase unwrapping, which leads to the creation of a displacement map, as shown in Figure 3.

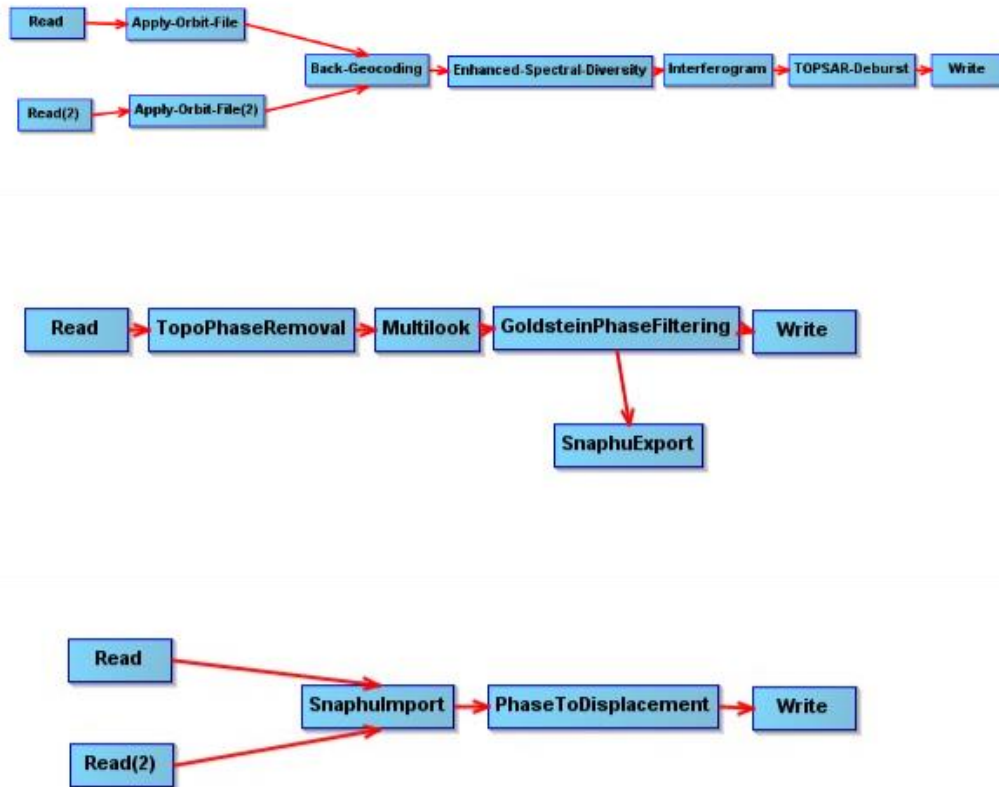


**Figure 3.** Three algorithms used for InSAR processing (the upper), DInSAR processing (the middle) and creating the Displacement map (the last)

### *Pre-processing step*

We open two products and split them. To reduce the processing time, we streamlined the following steps in the analysis: Select each image separately when saving the split product, and for the processing parameters, select sub-swath 1 and the polarization VV, and define the bars.

### *InSAR Processing*

InSAR Processing. First, we download split data and open it in SNAP, and the 1st step is InSAR Processing (gathering the phase information) between the two images. Here, the final product will be the interferogram, the phase difference between two images, which encompasses both topographic features and deformation, along with an estimation of image coherence.

### *DInSAR Processing*

Then, we will continue with the second processing, DInSAR Processing. The output product generated in this case will be the differential interferogram, which isolates the deformation by removing the topographic effects from the original interferogram.

### *Phase Unwrapping*

Phase Unwrapping and displacement map. In the 3rd processing part, Phase Unwrapping, we will include the phase and unwrapping to accurately derive the displacement measurements. Of course, there will be a geocoding of the product to finally generate the terrain-corrected displacement map, accounting for surface variations.

## RESULTS

### *Pre-processing step*

First, we begin by opening and viewing the two Sentinel-1 products in the Sentinel-1 Toolbox. In the Bands folder, we will find bands containing the real (i) and imaginary (q) parts of the complex data. The real and imaginary bands are the actual data in the product, while the Virtual Intensity band helps us work with and visualize the complex data.

Next, we open the two products and split them to reduce processing time in the next steps. For each image, we select it separately when saving the split product. In the processing parameters, we choose sub-swath 1 and VV polarization, and we define the bars for the image. The extent of the image is shown in red, and the selected bars are displayed in white.

After setting the parameters, we run the process to obtain the split products in SNAP. If we open the bands, we will only see IW 1, which corresponds to our region of interest. We repeat this process for each of the two products.

At this point, we now have two split products ready for further processing, see Figure 4.

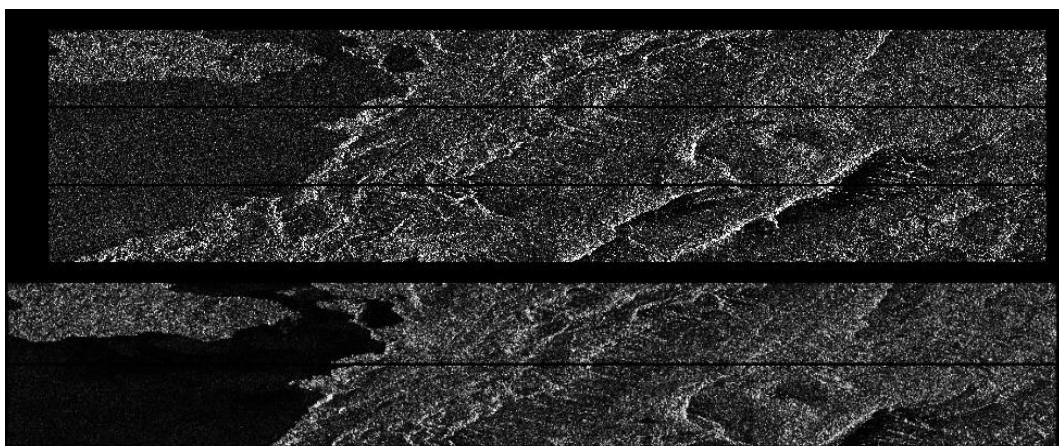


**Figure 4.** Pre-processing of two images and splitting the products

### *InSAR Processing*

We begin the analysis by setting up the processing graph in the Sentinel-1 Toolbox, defining the sequence of operations for the radar images. After adding the input and future output operators, we apply orbit files to ensure accurate satellite positioning. Next, we perform back-geocoding to perform image co-registration using a Digital Elevation Model (DEM), ensuring proper spatial alignment. Enhanced Spectral Diversity (ESD) is then used to correct range and azimuth differences in the images, improving data quality. With corrections made, we generate the interferogram by comparing the phase shifts between the images, revealing changes in the terrain. We then use TOPSAR Deburst to resample the images for consistent alignment across sub-swaths. Once processing is complete, we save the final interferogram and coherence map, which show surface deformation and data quality, respectively. The final product is saved under the name `_split_Orb_Stack_Ifg_Deb`. If we expand the bands, we have two new bands: the interferometric and the coherence. We have produced the interferogram, which contains both topography and deformation, see Figure 5.

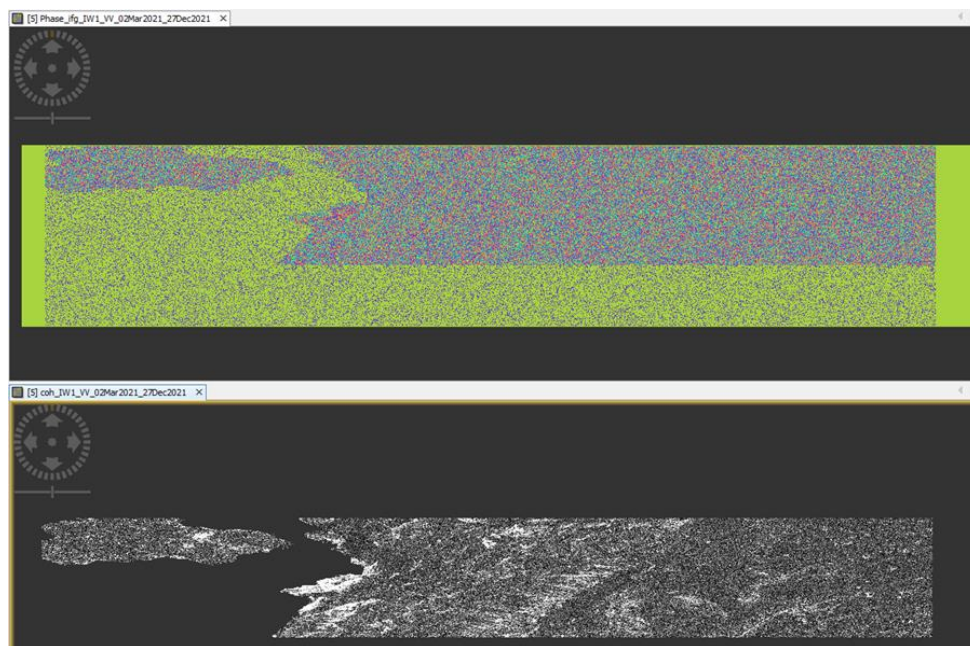


Figure 5. Phase and coherence

### *DInSAR Processing*

In the second part of the differential interferometry process, we create a differential interferogram that highlights deformation by comparing the phase shifts between two SAR images captured at different time intervals. First, we import the deburst interferogram containing the initial phase data. Then, we eliminate the topographic phase to isolate the deformation using the TopoPhaseRemoval operator, keeping default settings. To reduce

noise, we apply multilook processing with a range of 8 and azimuth of 2, resulting in a pixel size of 30.6. Next, we filter the phase using Goldstein Filtering to enhance the deformation signal, setting the Adaptive Filter Exponent to 1.0. After filtering, we save the processed interferogram as a multilooked and filtered product. We then export the data for SNAPHU phase unwrapping using the MCF method. Finally, we examine the results in the Product Explorer, where we can view the phase as fringes representing deformation, with closer fringes indicating greater change. We can also review the removed topographic phase by viewing the "topo\_phase" band, see Figure 6.

This differential interferogram provides valuable information pertaining to surface deformation, encompassing both the intensity and direction of motion. It can also be used to analyze parameters such as energy release and shaking intensity across the affected area.

Finally, the coherence histogram shows that the image pair used (from March 2, 2021, and December 28, 2021) shows significant coherence differences, indicating it meets the criteria for displacement analysis, see Figure 7.

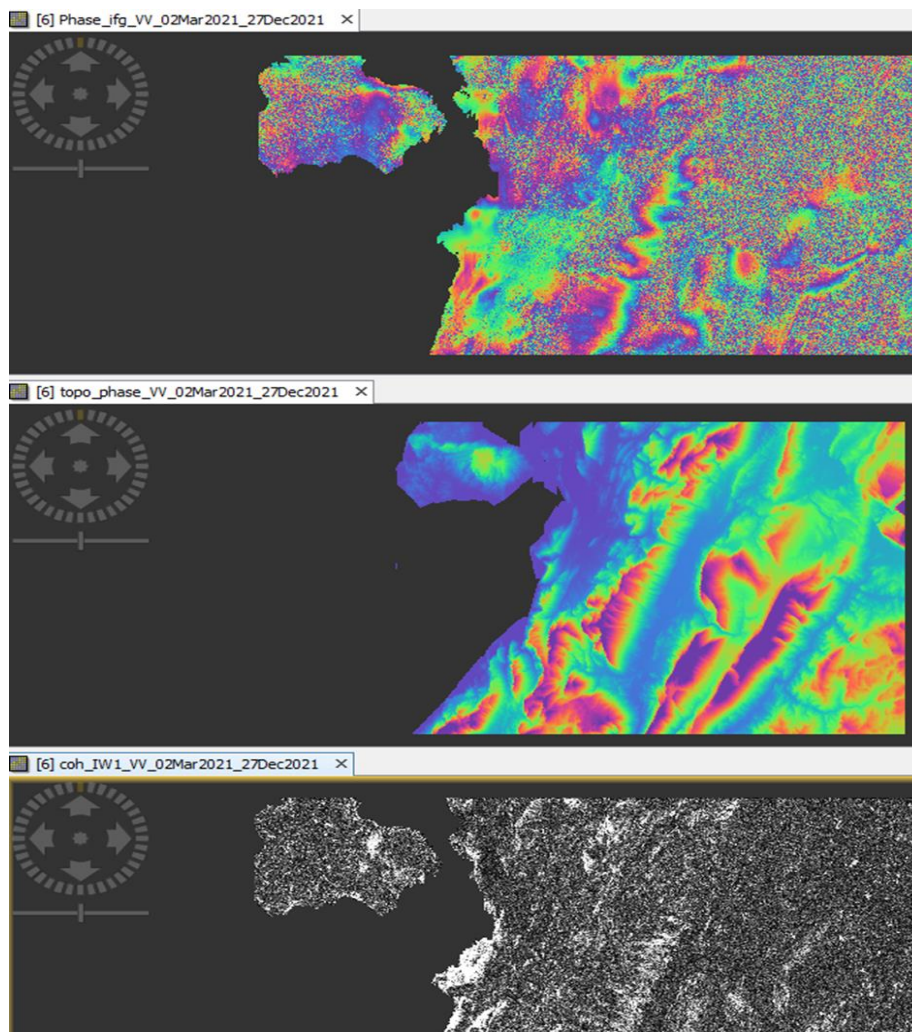


**Figure 6.** Phase, Topophase, and coherence bands

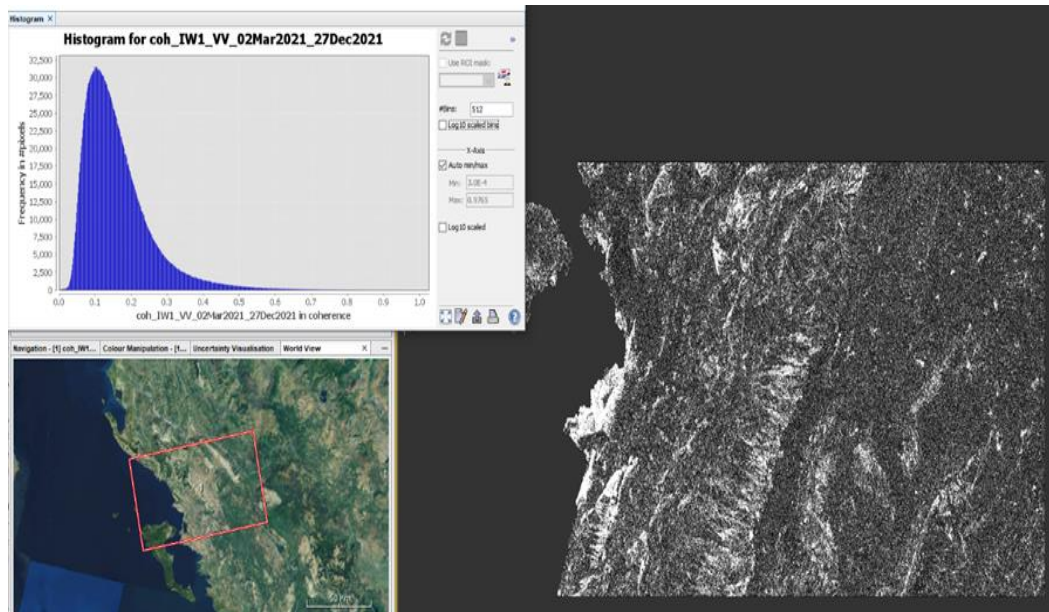


Figure 7. DInSAR coherence histograms of the study area: Coherence vs. frequency in pixels

### *Phase Unwrapping and Displacement Map*

Now, we will proceed with the third processing part: phase unwrapping and displacement measurements. Phase unwrapping is considered the most challenging part of interferometric data processing. For this study, we will utilize SNAPHU, a two-dimensional phase unwrapping algorithm.

We have done the Snaphu export, and we have to do Snaphu unwrapping and Snaphu import. If we open the Snaphu folder (target folder), where the data was exported for the Snaphu process. In the target folder, we have files that should be opened in the Snaphu program. To complete the phase unwrapping, we open a terminal window.

To proceed with phase unwrapping using SNAPHU, first, open a Linux terminal and navigate to the directory where the final product is located. Next, open the "snaphu.conf", which is a configuration file. Then copy the following command to call "snaphu": `snaphu -f snaphu.conf Phase_ifg_VV_02mar2021_27Dec2021.snaphu.img 2869`. Once it's open, we execute the necessary phase unwrapping process. Be sure to comment out the LOGFILE line by adding a "#" before it. After this, run the process, and the results will be stored in the specified folder, see Figure 8.

The algorithm processes the wrapped and unwrapped images using several operators: read for the wrapped image, read (2) for the unwrapped image, Snaphu Import, PhaseToDisplacement, and Write. We begin by selecting the differential interferogram (`_Ifg_Deb_DInSAR_ML_Flt`) and the unwrapped phase file (`_UnwPhase_ifg_VV_02mar2021_27Dec2021.snaphu.hdr`). The first step is importing the SNAPHU results to construct the interferometric product with the unwrapped phase band

and metadata. Next, we convert the phase to displacement, producing the displacement product. Finally, we use the Write operator to save the output as `_Ifg_Deb_DInSAR_ML_Flt_Displacement`. The product has one displacement band, viewable in the Product Explorer. Using the color manipulation tab, we adjust the display: red for -0.1 meters, white for 0 meters, and blue for +0.1 meters.

Since the product is in SAR geometry, project the data to map geometry using the Range Doppler Terrain Correction operator for geocoding. After applying terrain correction, the final product (`_Disp_TC`) contains the orthorectified `Displacement_VV` band. This can be displayed in Google Earth by saving it as `.kmz` (see Figures 9 & 10) and used to generate a displacement profile as can be depicted at Figure 11.

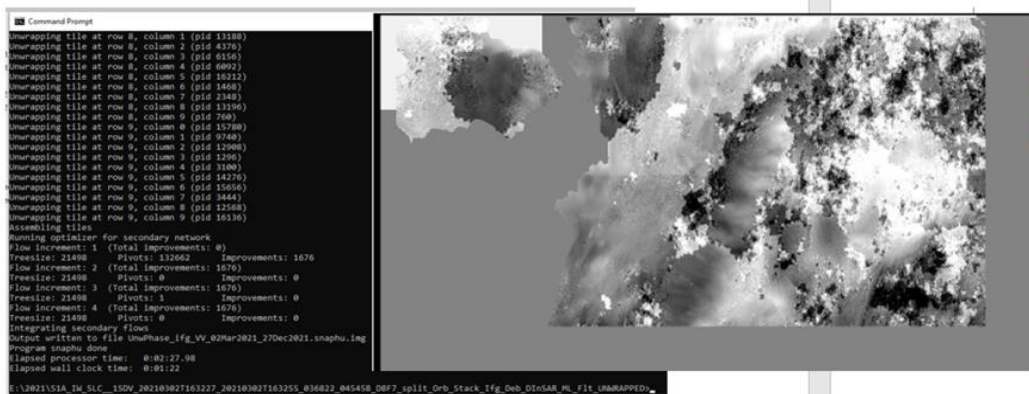


Figure 8. Phase Unwrapping

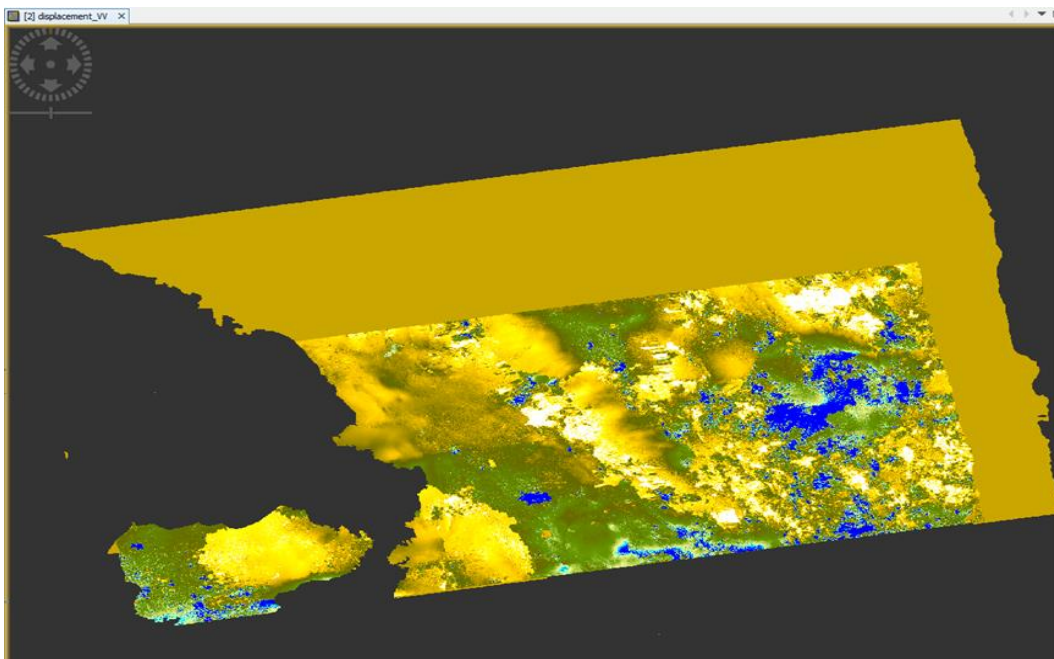


Figure 9. Displacement map after terrain correction



Figure 10. Displacement map in Google Earth

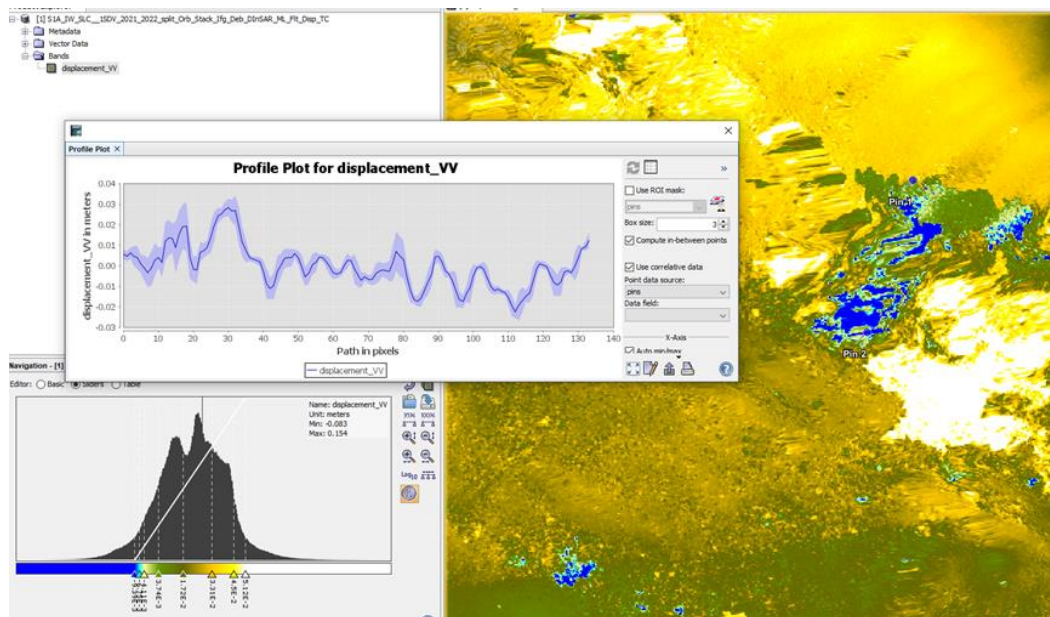


Figure 11. Profile plot for displacements in two selected points

## DISCUSSION

Although the study initially focused on a small area, the data collected covered a much larger region, providing valuable insights. This discussion outlines the process of generating the displacement map, which accurately reveals displacement patterns during the study period. Radar, or Radio Detection and Ranging, measures distance by

transmitting an electromagnetic signal and receiving the reflected echo. SAR, a specific radar system, uses platform movement and advanced signal processing to produce high-resolution images.

### *InSAR Processing*

InSAR maps ground deformation using radar images from orbiting satellites. In contrast to visible or infrared light, radar can penetrate through clouds and function in the dark, making it reliable in all weather conditions. Interferometry compares radar images taken at different times or from different positions, focusing on time differences in our study. Phase differences between these images create an interferogram, revealing the geometry of the scene. By removing topographic and orbital effects, we isolate ground movements along the radar's line of sight [27-29]. InSAR has been useful in studying landslides and monitoring regional deformation [30, 31].

In recent decades, various interferometric techniques, such as two-pass interferometry, interferometric stacking, Persistent Scatterer Interferometry (PSI), and Small Baseline Subsets (SBAS), have been developed for processing multi-temporal SAR data over large areas [29]. By analyzing radar images taken at different times from comparable viewpoints, the movement of the ground toward or away from the satellite can be quantified, generating a deformation map. Radar pulses are reflected off the Earth's surface and captured by the satellite, providing amplitude and phase information. Amplitude shows signal strength, while phase measures distance, and differences between images reveal changes in the surface. Combining the images, or "interfering," either reinforces or cancels the waves based on phase differences.

Orbit auxiliary data provide the satellite's position while acquiring SAR data and are automatically downloaded by Sentinel-1 Toolbox. The Precise Orbit Determination (POD) service provides POE files, which contain orbit state vectors at 10-second intervals for 28 hours, delivered within 20 days. Coregistration aligns the images with sub-pixel accuracy, ensuring both images (master and slave) match ground targets at the same pixel. A back-geocoding operator leverages satellite orbits and a digital elevation model for this process, masking out areas without coverage. Enhanced Spectral Diversity (ESD) is applied to improve coregistration, correcting range and azimuth discrepancies. An interferogram is created by multiplying the master image with the complex conjugate of the slave image, calculating phase differences that reflect the travel path variations between acquisitions.

During interferometric processing, we eliminate error sources to isolate surface deformation. Flat-earth phase removal, applied automatically during the creation of the interferogram, subtracts phase caused by the Earth's curvature using orbital and metadata information. Coherence between the reference and secondary images assesses phase quality, indicating how similar the images are and whether they're suitable for processing. Loss of coherence, caused by factors like temporal changes, geometric errors, and volumetric decorrelation, can degrade results. The interferogram's phase band shows phase differences and pixel similarity, with coherence values ranging from 0 to 1. High

coherence areas, like urban regions, appear bright, while low coherence areas, like vegetation, appear dark.

We proceed with the Sentinel-1 TOPSAR Deburst step. Each sub-swath is made up of multiple bursts, which are processed individually as separate SLC images. These individual bursts are then merged into a single sub-swath image, with black-fill boundaries between them. The overlap ensures continuous ground coverage.

In interferometry, fringes signify a  $2\pi$  phase change, with each cycle representing half the wavelength of the sensor. Ground movement is measured by counting the fringes and multiplying by half the wavelength. A higher density of fringes suggests greater deformation. In flat terrain, fringes remain constant or vary slowly. Deviations from parallel fringes indicate deformation.

After creating the interferogram, expand it and double-click the Phase\_... band to visualize the phase. Zooming in may reveal demarcation zones, which are removed after applying the TOPSAR Deburst operator, seamlessly joining the bursts.

### *DInSAR Processing*

DInSAR is an active remote sensing technique that examines phase differences between SAR images of the same scene, taken from similar geometries [32-35]. Using a multi-pass approach with a large dataset improves atmospheric and topographic phase estimates, reducing errors [36, 37]. To highlight deformation, the topographic phase is eliminated with a reference DEM using the Topographic Phase Removal operator in Sentinel-1 Toolbox. The interferometric phase can be affected by noise from decorrelation and scattering, so multi-looking is applied to improve signal-to-noise ratio and phase accuracy. Coherence, essential for unwrapping and deformation mapping, helps assess phase quality; values below 0.3 are typically discarded. In the interferogram, coherence is strongest in urban areas and weakest in vegetated regions. The Goldstein filtering method is applied, revealing low coherence values between 0.1 and 0.2, indicating minimal similarity between image pairs [38].

### *Phase Unwrapping*

Phase unwrapping is necessary to recover the absolute phase by adding multiples of  $2\pi$  to the phase of each pixel, reconstructing the original signal. In this study, we use SNAPHU, a two-dimensional unwrapping algorithm, to make the phase continuous [39]. The interferometric phase is initially ambiguous, confined within a  $2\pi$  range, and needs to be unwrapped to correlate with topographic height. The altitude of ambiguity (ha) defines the altitude difference that results in a  $2\pi$  phase shift. Phase unwrapping addresses this by accumulating phase differences between neighbouring pixels. Phase-to-displacement conversion directly translates phase into meters, and terrain corrections are applied to compensate for distortions caused by topography and satellite sensor tilt. How does phase unwrapping affect the final displacement map?

Phase unwrapping plays a crucial role in determining the accuracy, reliability, and clarity of the resulting displacement map. When done correctly, it ensures precise identification of ground deformation, whereas poor unwrapping can lead to errors that undermine the analysis. This process converts relative displacement into absolute values, assisting in the reconstruction of the complete phase signal and enabling the computation of actual displacement. Errors during phase unwrapping, especially in areas with weak coherence, can spread and distort the entire displacement map. Ensuring accurate unwrapping is vital to maintain the integrity of deformation boundaries (such as those near a mining area). It also influences quantitative analysis, as displacement values are derived directly from the unwrapped phase.

Interferometric data generally faces three types of noise: phase noise from radar and wave propagation, height noise from uncertainties in the interferometer's dimensions, and geometric distortion from radar imaging [40, 41]. The most noticeable changes occur during the unwrapping stage, primarily due to the lower coherence in the Sentinel-1 Toolbox interferogram. To address this, it's necessary to mask low-coherence areas or use software with more accurate co-registration processors to improve coherence. If interpreting a deformation map with uncertain displacement calculations, the best way to verify displacement values is to compare them with known ground truth data.

Interferograms can also be affected by atmospheric conditions, especially water vapour, during acquisitions. Atmospheric errors remain even after masking low-coherence areas, as they only affect phase and distance measurements, not coherence [42].

What quality checks should be performed?

To ensure reliable displacement results, several quality control measures must be implemented. A coherence check must be performed to remove areas with low signal quality, preventing misleading data. The phase unwrapping process must be reviewed for errors or unnatural jumps that could distort displacement values.

Ground measurements, when available, must be compared with satellite data for accuracy verification. Noise reduction must be applied carefully to preserve true deformation signals while minimizing interference. Time series analysis must be conducted to ensure consistency across multiple images and confirm stable results over time. Finally, uncertainty estimation and consideration of the satellite's line of sight must be done to ensure accurate data interpretation, avoiding distortions from viewing angles.

## CONCLUSIONS

The findings of this study provide critical insights into both the magnitude and behaviour of surface deformation over time. This study demonstrates how interferometric processing can be used to observe and analyse relative surface deformations in the radar line-of-sight direction. When two observations are made from the same location at different times, the interferometric phase is directly related to changes in the range of a surface

feature. We identified areas exhibiting significant motion due to variations in the radar signal phase.

The detailed maps produced also reveal the spatial extent of deformation across the entire study area, enabling more precise localization of instability zones compared to conventional ground-based methods. Each stage of this process is crucial and demands precise interpretation, particularly when using the SNAPHU program. This study has also helped identify the area surrounding the former salt mine, contributing to a more accurate assessment of the situation when combined with other geological studies.

These results support a more comprehensive understanding of the processes involved, whether natural or human-induced. SAR interferometry is widely used for deformation mapping and change detection. The findings are vital for maintenance planning, risk assessment, and ensuring structural safety.

In the future research work, accurate displacement measurements can be achieved through post-processing techniques such as masking incoherent values and applying methods like vertical displacement estimation using band math. These techniques will be explored in future studies.

By integrating data from both ascending and descending satellite tracks, it becomes possible to more accurately estimate the vertical and horizontal components of displacement.

Additionally, InSAR time series analysis can help reduce the impact of atmospheric errors and determine whether the deformation is continuous, accelerating, seasonal, or episodic.

## CONFLICT OF INTERESTS

The authors state no conflict of interest.

## DATA AVAILABILITY STATEMENT

The datasets used in this study are provided by the European Space Agency within the Copernicus Programme and can be downloaded at <https://browser.dataspace.copernicus.eu/>

The following products were used:

S1A\_IW\_SLC\_\_1SDV\_20210302T163227\_20210302T163255\_036822\_04545B\_D8F7.SAF  
E 02/03/2021 (before the subsidence) and

S1A\_IW\_SLC\_\_1SDV\_20211227T163234\_20211227T163302\_041197\_04E53D\_E121.SAF  
E 27/12/2021(after the subsidence)

## REFERENCES

1. Cooper, A.H. Halite Karst Geohazards (Natural and Man-Made) in the United Kingdom, *Environmental Geology*, **2002**; 42(5); 505–512.

2. Reuter, F., Stoyan, D. Sinkholes in Carbonate, Sulfate and Chloride Karst Regions: Principles and Problems of Engineering-Geological Investigations and Predictions, *Proceedings of the Fourth Multidisciplinary Conference on Sinkholes and the Engineering and Environmental Impacts of Karst*, Panama City, 1993; A.A. Balkema, Rotterdam; pp. 45-54.
3. Gutierrez, F., Cooper, A.H. Evaporite Dissolution Subsidence in the Historical City of Calatayud, Spain: Damage Appraisal and Prevention, *Natural Hazards*, **2002**; 25(3); 259–288.
4. Veress, M. Development Environments and Factors of Subsidence Dolines, *Geosciences*, **2021**; 11(12); 513.
5. Dyagilev, R.A., Shulakov, D.Y., Butyrin, P.G. Seismicity Associated with Karst in Flooded Salt Mines in Perm Region, Russia, *8th International Symposium on Rockbursts and Seismicity in Mines*, Russia, **2013**; pp. 511-516.
6. Schuchová, K., Lenart, J. Geomorphology of Old and Abandoned Underground Mines: Review and Future Challenges, *Progress in Physical Geography: Earth and Environment*, **2020**; 44(6); 791–813.
7. Sahu, P., Lokhande, R.D. An Investigation of Sinkhole Subsidence and its Preventive Measures in Underground Coal Mining, *Procedia Earth and Planetary Science*, **2015**; 11(1); 63-75.
8. Alonso-Díaz, A., Casado-Rabasco, J., Solla, M., Lagüela, S. Using InSAR and GPR Techniques to Detect Subsidence: Application to the Coastal Area of "A Xunqueira" (NW Spain), *Remote Sensing*, **2023**; 15(15); 3729.
9. Barla, G., Tamburini, A., Del Conte, S., Giannico, C. InSAR Monitoring of Tunnel-Induced Ground Movements, *Geomechanics and Tunnelling*, **2016**; 9(1); 15–22.
10. Bock, Y., Wdowinski, S., Ferretti, A., Novali, F., Fumagalli, A. Recent Subsidence of the Venice Lagoon from Continuous GPS and Interferometric Synthetic Aperture Radar, *Geochemistry, Geophysics, Geosystems*, **2012**; 13(3); Q03023.
11. Carlà, T., Farina, P., Intrieri, E., Ketizmen, H., Casagli, N. Integration of Ground-Based Radar and Satellite InSAR Data for the Analysis of an Unexpected Slope Failure in an Open-Pit Mine, *Engineering Geology*, **2018**; 235(1); 39–52.
12. Carnec, C., Delacourt, C. Three Years of Mining Subsidence Monitored by SAR Interferometry, Near Gardanne, France, *Journal of Applied Geophysics*, **2000**; 43(1); 43–54.
13. Colesanti, C., Mouelic, S.L., Bennani, M., Raucoules, D., Carnec, C., Ferretti, A. Detection of Mining-Related Ground Instabilities Using the Permanent Scatterers Technique: A Case Study in the East of France, *International Journal of Remote Sensing*, **2005**; 26(1); 201–207.
14. Colombo, D., MacDonald, B. Using Advanced InSAR Techniques as a Remote Tool for Mine Site Monitoring, *Slope Stability Proceedings 2015*, The Southern African Institute of Mining and Metallurgy, **2015**; pp. 121–132.
15. Reilinger, R.E., Ergintav, S., Bürgmann, S., McClusky, S., et al. Coseismic and Postseismic Fault Slip for the 17 August 1999, M=7.5, Izmit, Turkey Earthquake, *Science*, **2000**; 289(5484); 1519-1524.
16. Pedersen, R., Sigmundsson, F., Feigl, K.L., Árnadóttir, T. Coseismic Interferograms of Two Ms=6.6 Earthquakes in the South Iceland Seismic Zone, June 2000, *Geophysical Research Letters*, **2001**; 28(17); 3341-3344.
17. Amelung, F., Galloway, D.L., Bell, J.W., Zebker, H.A., Lacznia, R.J. Sensing the Ups and Downs of Las Vegas: InSAR Reveals Structural Control of Land Subsidence and Aquifer System Deformation, *Geology*, **1999**; 27(6); 483-486.
18. Lu, Z.; Mann, D.; Freymueller, J.T.; Meyer, D.J. Synthetic Aperture Radar Interferometry of Okmok Volcano, Alaska: Radar Observations, *Journal of Geophysical Research*, **2000**; 105(B5); pp. 10791-10806.

19. Salvi, S., Atzori, S., Tolomei, C., Allievi, J., Ferretti, A., Rocca, F., Prati, C., Stramondo, S., Feuillet, N. The Inflation Rate of the Colli Albani Volcanic Complex Was Retrieved by the Permanent Scatterers SAR Interferometry Technique, *Geophysical Research Letters*, **2004**; 31(12); L12606.
20. Joughin, I., Fahnestock, M., Kwok, R., et al. Iceflow of Humboldt, Petermann, and Ryder Gletscher, Northern Greenland, *Journal of Glaciology*, **1999**; 45(150); pp. 231–241.
21. Mohr, J.J., Reeh, N., Madsen, S.N. Three-Dimensional Glacial Flow and Surface Elevation Measured with Radar Interferometry, *Nature*, **1998**; 391(6664); 273–276.
22. Delacourt, C., Allemand, P., Squarzoni, C., Picard, F., Raucoules, D., Carnec, C., Potential and limitations of ERS-Differential SAR Interferometry for landslide studies in the French Alps and Pyrenees, Proceedings of Fringe 2003 Workshop, SP-550, ESA (CD-ROM), **2004**.
23. Hilley, G.E., Bürgmann, R., Ferretti, A., Novali, F., Rocca, F., Dynamics of Slow-Moving Landslides from Permanent Scatterer Analysis, *Science*, **2004**; 304; pp. 1952–1955.
24. Crosetto, M., Castillo, M., Arbiol, R., Urban subsidence monitoring using radar interferometry: Algorithms and validation, *Photogrammetric Engineering and Remote Sensing*, **2003**; 69(7); 775–783.
25. Lanari, R., Mora, O., Manunta, M., Mallorquí, J.J., Berardino, P., Sansosti, E., A small-baseline approach for investigating deformations on full-resolution differential SAR interferograms, *IEEE Transactions on Geosciences and Remote Sensing*, **2004**; 42(7); 1377–1386.
26. Copernicus database. Available from: <https://dataspace.copernicus.eu/browser> (accessed on 20 January 2025)
27. Xu, Y., Lu, Z., Schulz, W.H., Kim, J., Twelve-year dynamics and rainfall thresholds for alternating creep and rapid movement of the Hooskanaden landslide from integrating InSAR, pixel offset tracking, and borehole and hydrological measurements, *J. Geophys. Res.*, **2020**; 125; e2020JF005640.
28. Wasowski, J., Bovenga, F., Investigating landslides and unstable slopes with satellite Multi-Temporal Interferometry: current issues and future perspectives, *Eng. Geol.*, **2014**; 174; 103–138.
29. Solari, L., Bianchini, S., Franceschini, R., Barra, A., Monserrat, O., Thuegaz, P., Bertolo, D., Crosetto, M., Catani, F. Satellite interferometric data for landslide intensity evaluation in mountainous regions, *Int. J. Appl. Earth Obs. Geoinf.*, **2020**; 87; 102028.
30. Zhang, Y., Meng, X.M., Dijkstra, T.A., Jordan, C.G., Chen, G., Zeng, R.Q., Novellino, A., Forecasting the magnitude of potential landslides based on InSAR techniques, *Remote Sens. Environ.*, **2020**; 241; 111738.
31. Dini, B., Manconi, A., Loew, S., Investigation of slope instabilities in NW Bhutan as derived from systematic DInSAR analyses, *Eng. Geol.*, **2019**; 259; 105111.
32. Zhao, C., Lu, Z., Zhang, Q., de La Fuente, J., Large-area landslide detection and monitoring with ALOS/PALSAR imagery data over northern California and southern Oregon, USA, *Remote Sens. Environ.*, **2012**; 124; 348–359.
33. Ferretti, A., Monti-Guarnieri, A., Prati, C., Rocca, F., InSAR Principles: Guidelines for SAR Interferometry Processing and Interpretation; European Space Agency: Paris, France, **2007**.
34. Veci, L., Sentinel-1 Toolbox—TOPS Interferometry Tutorial; European Space Agency; Array Systems Computing Inc.: Toronto, ON, Canada, **2016**.
35. Braun, A., Veci, L., Sentinel-1 Toolbox—TOPS Interferometry Tutorial; European Space Agency; SkyWatch Space Applications Inc.: Waterloo, ON, Canada, **2020**.
36. Zebker, H.A., Rosen, P.A., Hensley, S., Atmospheric Effects in Interferometric Synthetic Aperture Radar Surface Deformation and Topographic Maps, *J. Geophys. Res. Solid Earth*, **1997**; 102; 7547–7563.

37. Yu, C., Li, Z., Penna, N.T., Interferometric Synthetic Aperture Radar Atmospheric Correction Using a GPS-Based Iterative Tropospheric Decomposition Model, *Remote Sens. Environ.*, **2018**; 204; 109–121.
38. Goldstein, R.M., et al., Radar interferogram filtering for geophysical applications, *Geophysical Research Letters*, **1998**.
39. Chen, C.W., Zebker, H.A., Phase Unwrapping for Large SAR Interferograms: Statistical Segmentation and Generalized Network Models, *IEEE Transactions on Geoscience and Remote Sensing*, **2002**; 40; 1709–1719.
40. Bürgmann, R., Rosen, P.A., Fielding, E.J., Synthetic aperture radar interferometry to measure Earth's surface topography and its deformation, *Annual Review of Earth and Planetary Sciences*, **2000**; 28; 169–209.
41. Rosen, P.A., Hensley, S., Joughin, I.R., Li, F.K., Madsen, S.N.; Rodriguez, E.; Goldstein, R.M., Synthetic aperture radar interferometry, *Proceedings of the IEEE*, **2000**; 88(3); pp. 333–382.
42. Nonaka, T., Asaka, T., Iwashita, K., Evaluation of Atmospheric Effects on Interferograms Using DEM Errors of Fixed Ground Points, *Sensors*, **2018**; 18(7); 2336.